conference papers

Structural changes in gradient colloidal thin gold films deposited from aqueous solution

S. V. Roth,[a]* P. Müller-Buschbaum,[b] A. Timmann,[a] J. Perlich[b] and R. Gehrke[a]

[a]HASYLAB at DESY, Notkestr. 85, D-22607 Hamburg, Germany, and [b]Physik-Department LS E13, Technische Universität München, James-Franck-Str. 1, D-85748 Garching, Germany. Correspondence e-mail: stephan.roth@desy.de

Pattern formation is investigated in a one-dimensional gradient prepared from an aqueous colloidal gold nanoparticle solution. The hydrodynamic process can be reconstructed by determining the prominent length scales and surface roughness in the dried gradient. The structural information is obtained using a combination of grazing-incidence small-angle X-ray scattering, which is a method of high-statistical relevance, and a moderate microfocused beam. This allows for scanning the gradient and to locally reveal the structure of the thin film. Our results, based on a simplified hydrodynamic model, indicate a system oscillating between depleted regions, nanoparticle domains and complete nanoparticle layers.

1. Introduction

Nano-structured noble metal thin films are of great scientific and technological importance (Bauer *et al.*, 2003; de Heer *et al.*1987; Ditlbacher *et al.*, 2000; Schmid & Chi, 1998; Jin *et al.*, 2001; Maier *et al.*, 2001). They play a major role in biotechnology, *e.g.* DNA scanning (Vo-Dinh *et al.*, 1999; Dubertret *et al.*, 2001; Bauer *et al.*, 1999; Taton *et al.*, 2000), in solar cells (Westphalen *et al.*, 2000; Stenzel *et al.*, 1995), anti-counterfeiting (Bauer *et al.*, 2003) and optical data storage (Ditlbacher *et al.*, 2000). These areas of research and applied science exploit the so-called 'plasmon resonance' of the noble metal nano-particles. It occurs due the excitation of free electron gas in the confinement of the nanoparticle (Zeman & Schatz, 1987; Hulteen *et al.*, 1997). The plasmon resonance leads to distinct extinction bands in the optical spectrum. The field enhancement accompanying the resonance can be exploited *e.g.* in solar cells to increase efficiency (Westphalen *et al.*, 2000), in optical filters (Park & Xia, 1999) or to detect single molecules, using surface enhanced Raman spectroscopy (Garell, 1989). All of these methods rely upon a nanostructured noble metal layer on top of a highly reflecting substrate.

The spectral width and energy of the plasmon resonance strongly depends upon the nanoparticle morphology and the noble metal layer's structure (Hulteen *et al.*, 1997). Deposition methods of choice include vapour deposition techniques (Roth *et al.*, 2003; Bhat *et al.*, 2003), sputtering (Roth, Walter *et al.*, 2006; Bauer *et al.*, 2003), pulsed laser deposition (Krebs *et al.*, 2003) and solution casting (Park & Xia, 1999; Su, 2004; Narayanan *et al.*, 2004). All these methods aim to produce a large and homogeneous surface area. However, for combinatorial investigations (Roth *et al.*, 2003; Roth, Walter *et al.*, 2006), it is often useful to install several morphologies on one single sample. This is frequently achieved by creating a gradient for one specific parameter, such as concentration or thickness. These one-dimensional gradients can then be investigated *via* high-throughput methods. This allows several morphologies, prepared under identical conditions, to be screened. Gradients are typically installed by deposition from a vapour phase. However, within this work we concentrate on solution deposition, based on a colloidal nanoparticle

solution. Microbeam grazing-incidence small-angle X-ray scattering (μGISAXS) (Roth *et al.*, 2003; Roth, Walter *et al.*, 2006; Müller-Buschbaum *et al.*, 2003) is used for the *ex-situ* investigation of a one-dimensional gradient of nearly monodisperse gold nanoparticles. The gradient was created by a solution casting technique, followed by drying. The results presented here indicate a crossover and oscillation from a homogeneous layer to depleted regions due to capillary forces (Denkov *et al.*, 1993).

This paper is structured as follows. In the first experimental part we describe sample preparation. In the second experimental part we introduce the measuring technique, namely μGISAXS. In the third section we present a semi-quantitative analysis of the experiment by extracting the most prominent length scales present along the gradient. A fully quantitative analysis, as *e.g.* carried out by Revenant *et al.* (2004), is beyond the scope of this paper. We finalize our paper with a conclusion of this combinatorial study.

2. Experimental part I: sample preparation

Solution casting was performed using a colloidal gold solution (Kisker Biotechnologie). The gold nanoparticles with a nominal diameter of 5.4 nm were in an aqueous solution with a concentration of 5×10^{13} particles ml^{-1}. Silicon wafers with (111) orientation (Si-Mat, Landsberg, Germany) were used as substrate for the nano-particle layer. The wafers were cleaned in an acid bath to ensure a well defined oxide layer. The acid bath consisted of a solution containing 110 ml deionized water, 160 ml sulfuric acid and 70 ml hydrogen peroxide at 353 K. The wafers were cleaned in the bath for 15 min, and afterwards rinsed several times with deionized water before being dried carefully in a nitrogen atmosphere.

A one-dimensional gradient was created using a new geometry as shown in Fig. 1. Part of the surface of the cleaned wafer was covered with a second wafer piece to install a barrier against liquid flow. A drop (diameter 3 mm) of colloidal solution was deposited on the uncovered part of the base wafer surface using a syringe. The drop immediately wets the surface until it encounters the barrier and
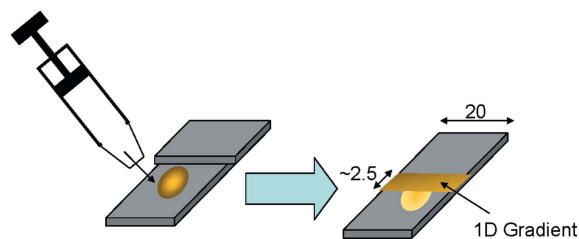
Figure 1
Sketch of the applied sample preparation to install a one-dimensional (1D) gradient (length ~20 mm, width ~2.5 mm). The initial droplet and the wetted area including the one-dimensional gradient are indicated. The extension of the one-dimensional gradient is approximately 2.5 mm.

thereby installs a thin solution film. This thin film dries by evaporation of the solvent water (Denkov *et al.*, 1992; Denkov *et al.*, 1993; Deegan *et al.*, 1997; Deegan, 2000). Due to the increased amount of colloidal solution near the barrier and the pinning of the three-phase contact line at the barrier, a one-dimensional concentration gradient in close vicinity to the barrier is installed. This is in contrast to drying drops, where typical ring-shaped patterns were observed (Deegan *et al.*, 1997; Deegan, 2000, Su *et al.*, 2004). Similar to drying drops, the patterned regions are small compared with the wetted area. After a drying for 22 h under controlled conditions (room temperature and a humidity of 78%), all the water was completely evaporated, having creating a one-dimensional gradient. Finally the barrier is lifted off.

3. Experimental part II: microbeam grazing-incidence small-angle X-ray scattering

Structural changes across the one-dimensional gradient were investigated using an advanced X-ray scanning technique, namely microbeam grazing-incidence small-angle X-ray scattering (Roth *et al.*, 2003; Roth, Walter *et al.*, 2006; Müller-Buschbaum *et al.*, 2003). The experiments were carried out at beamline BW4 of HASYLAB/DESY (Gehrke, 1992; Roth, Döhrmann *et al.*, 2006). BW4 is a dedicated materials science beamline with focus on grazing-incidence techniques. Being initially designed as an ultra-small-angle X-ray scattering (USAXS) beamline, an ongoing upgrade led to the installation of dedicated SAXS stations with sample-to-detector
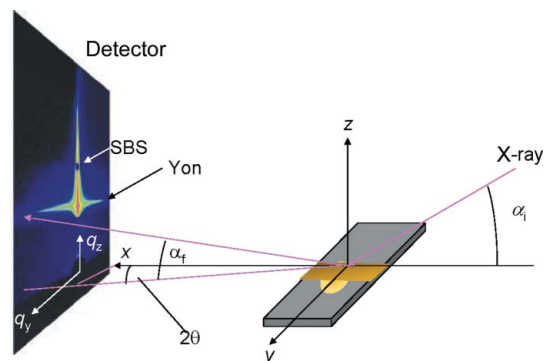

Figure 2
Scattering geometry of the µGISAXS experiment. α_i is incident angle, α_f is exit angle, 2θ is out-of-plane angle. x, y and z denote a Cartesian coordinate system and q_y and q_z a reciprocal space coordinate system. q_y and q_z are the components of the wavevector transfer parallel and vertical to the sample surface and are defined as $q_z = 2\pi/\lambda(\sin\alpha_i + \sin\alpha_f)$ and $q_y \simeq 2\pi/\lambda\sin2\theta$ with λ being the wavelength. The µGISAXS data are recorded on a two-dimensional detector. SBS denotes the specular beam stop and Yon the Yoneda peak.

distances SDD <4 m to increase the accessible q-range. q is the modulus of the scattering vector and defined as $q = (4\pi/\lambda)\sin\theta$, where λ is the wavelength and θ is half the scattering angle. Owing to its high flux given by the wiggler source and high resolution and stability, BW4 has been shown to be capable of performing microbeam experiments using beryllium compound refractive lenses (BeCRLs) (Schroer *et al.*, 2006; Roth, Döhrmann *et al.*, 2006).

For the *ex-situ* experiments described here, the incident X-ray beam was collimated using a slit system 20 m from the wiggler source (slit opening: 0.8×0.4 mm², horizontal × vertical, h x v). The beam was then focused using a set of 15 parabolic BeCRLs (Lengeler *et al.*, 2005) yielding a focal spot size of 71×60 µm² (h × v). The parameters of the parabolic BeCRLs were an aperture of 0.8 mm and a radius of 0.208 mm (Lengeler *et al.*, 2005). The achieved beam size in the focus allows lateral scanning of heterogeneous samples. This moderate microbeam was combined with a reflection setup used for GISAXS experiments. This method has been described previously (Roth *et al.*, 2003; Roth, Walter *et al.*, 2006; Müller-Buschbaum *et al.*, 2003; Roth *et al.*, 2004; Müller-Buschbaum *et al.*, 2006). Thus we introduced µGISAXS – GISAXS with microbeams – at BW4. The wavelength used was $\lambda = 1.38$ Å and the sample-to-detector distance, SDD = 2063 mm. The detector was a two-dimensional charge-coupled device detector (Mar Research) with 2048×2048 pixels and a pixel size of 79.1 µm. Upstream of the sample, a guard slit was installed to suppress parasitic scattering. The incident beam was monitored using ionization chambers.

Fig. 2 shows the schematic setup of the µGISAXS experiment including a typical µGISAXS pattern in the two-dimensional detector plane. The X-ray beam impinges onto the sample at an incident angle of $\alpha_i = 0.7°$. Specular and diffuse scattering contributions are observed. The exit angle with respect to plane defined by the sample surface normal (parallel to the z-direction) and the incident beam is denoted by α_f, the out-of-plane angle is denoted as 2θ. Both direct and specular reflected beams are blocked by two separate point-like beam stops to avoid overexposure of the detector. Owing to the small beam size, the footprint on the sample is only 0.071×4.9 mm² (h × v). Thus it is well suited for lateral scanning of one-dimensional gradients. Thus the gradient was placed parallel to the y-direction perpendicular to the beam. The step size was $\Delta y = 150$ µm, in order to scan a large area of several mm.

A typical µGISAXS pattern is shown in Fig. 2. Included is a reciprocal space coordinate system (q_y, q_z). q_y and q_z denote the components of the wavevector parallel and perpendicular to the surface, respectively, with $q_z = 2\pi/\lambda(\sin\alpha_i + \sin\alpha_f)$ and $q_y \simeq 2\pi/\lambda\sin2\theta$. Hence the off-specular intensity contains the structural (distance between isolated objects D) and morphological information (shape of the individual objects) (Salditt *et al.*, 1995; Naudon & Thiaudière, 1996). The two-dimensional data can then be analyzed in terms of so-called out-of-plane cuts and detector cuts (Müller-Buschbaum, 2003). It is worthwhile to note, that the term 'out-of-plane' refers to the scattering plane defined by the incoming beam and the surface normal. Thus, this cut is parallel to the sample surface, whereas the detector cut is perpendicular to it. A detector cut along q_z at $q_y = 0$ reveals correlations vertical to the sample surface. This includes resonant diffuse scattering (Müller-Buschbaum, 2003) and the so-called Yoneda peak (Yoneda, 1963). The Yoneda peak arises due to an interference effect of the incident and scattered wave. If $\alpha_{i,f} = \alpha_c$, the field is enhanced to twice the incident field because the standing wavefield of the incident and reflected waves reach their maximum. α_c denotes the critical angle of the materials involved and can be calculated from the real part of the refractive index δ as $\alpha_c = (2\delta)^{0.5}$. In the case of silicon this angle is $\alpha_c(Si) = 0.2°$. In a so-called out-of-
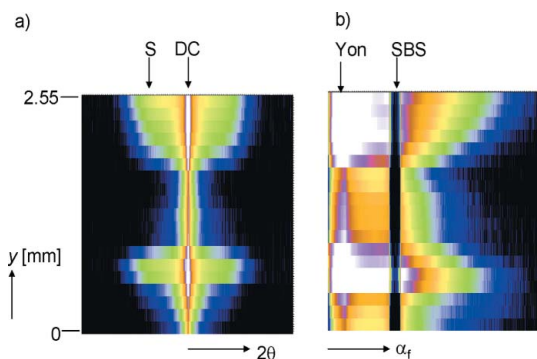
Figure 3
(a) Mapping of the out-of-plane cuts. The scan direction is y (step size Δy = 150 μm). The scanning range of 2.5 mm is indicated. S denotes the position of the correlation maxima (distance d_S) of the gold nanoparticles. DC notes the position of the detector cut in (b) (2θ = 0°, q_y = 0, respectively). (b) Mapping of the detector cuts. SBS denotes the specular beamstop, Yon the Yoneda maxima of silicon ($α_f$ = 0.2°). In both cases the intensity is shown on a logarithmic scale and is adapted to put emphasis on the visibility of the reported features. The out-of-plane cuts in (a) were done at the position Yon, i.e. the critical angle of silicon.

plane cut along q_y at fixed q_z correlations parallel to the sample surface are detected. In the case of nanoparticles the occurrence of side maxima in q_y allows determination of their most prominent distances approximately in a very simple approach via

$$d \approx 2\pi/q_y. \tag{1}$$

A more elaborate approach would include a detailed modelling of shape and shape distribution of the particles (Roth et al., 2003; Roth, Walter et al., 2006; Revenant et al., 2004).

4. Results and discussion

Fig. 3(a) shows a map of the out-of-plane cuts at each scan position along y. Two exemplary two-dimensional μGISAXS patterns are shown as insets in Fig. 4. All intensities are normalized to the incoming flux. In the presentation chosen in Fig. 3(a), all cuts at q_z corresponding to $α_c$(Si) as a function of 2θ are mapped in one single plot. From these cuts, the most-prominent in-plane length scales are determined and displayed as a function of the scan position y in Fig. 4(a). The y axis is defined with the barrier being at y = 0 mm. A clear change in the diffusively scattered signal is visible. The intensity oscillates between large 2θ values indicating a change from small correlation distances ($d_S \simeq 10$ nm at e.g. y = 0.65 mm) to large correlation distances (d_L is of the order of 100 nm) e.g. at y = 1.05 mm). The corresponding mapping of the detector cuts in Fig. 3(b) correlate well with the out-of-plane map. In the region where short correlation distances prevail, the diffusively scattered radiation between the Yoneda and specular peak is increased. This indicates an increased surface roughness, induced by packing the nanoparticles with distance d_S. The decrease of this diffuse intensity in regions where no small correlation distances are observed indicates a depleted nanoparticle region. This qualitative analysis already shows the existence of a one-dimensional concentration gradient.

Fig. 4(a) presents the semi-quantitative analysis of the flow processes involved in establishing the one-dimensional gradient. From the out-of-plane cuts the position of side maxima can be determined. Using equation (1) the most-prominent in plane length can be calculated. The vertical error bar indicates the fitting error, while the horizontal error bar takes into account the beam size
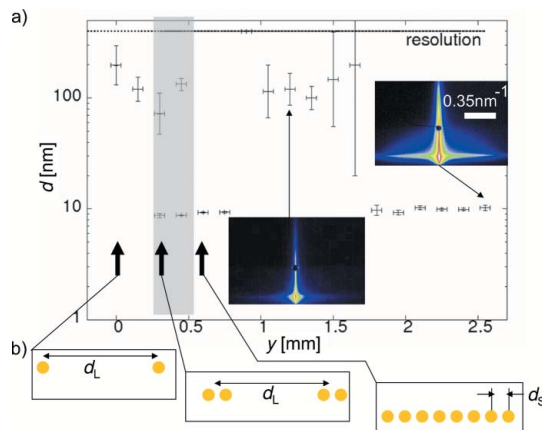

Figure 4
Crossover regimes in the one-dimensional gradient. (a) Plot of the most prominent in-plane length scales as a function of the scan position y. Two typical two-dimensional μGISAXS patterns at y = 0.65 mm and y = 2.55 mm are shown as insets. (b) Schematic representation of transition from largely separated nanoparticles (distance d_S) to packed nanoparticles with distance d_S approximately twice the nanoparticle diameter. The grey shaded region indicates a cross-over regime where domains (distance d_L) of nanoparticles, being separated by d_S, have formed.

(defining the area over which is averaged the scattering experiment). Two length scales prevail: d_L is of the order of 100 nm indicating largely separated nanoparticles and $d_S \simeq 10$ nm indicating nearest neighbour distances between individual gold nanoparticles of 5.4 nm diameter. In order to make the maxima evident, Fig. 5 shows the out-of-plane cut for the two-dimensional μGISAXS pattern shown in Fig. 4(a). The maxima corresponding to d_L and d_S are clearly visible.

Based on earlier work (Govor et al., 2004; Deegan et al., 1997; Deegan, 2000; Denkov et al., 1992; Denkov et al., 1993), we establish a simple qualitative model for the structure formation. With the barrier placed at y = 0 mm, first a drop of colloidal solution is deposited on the substrate at a position y = 5 mm. The drop wets the cleaned Si surface until it hits the barrier. This leads to an increased amount of solution in the vicinity of the barrier. Immediately after deposition, solvent evaporation sets in. This leads to a backflow of colloidal nanoparticles from the barrier in the direction of the drop position. The drop itself can be regarded as a reservoir delivering colloidal
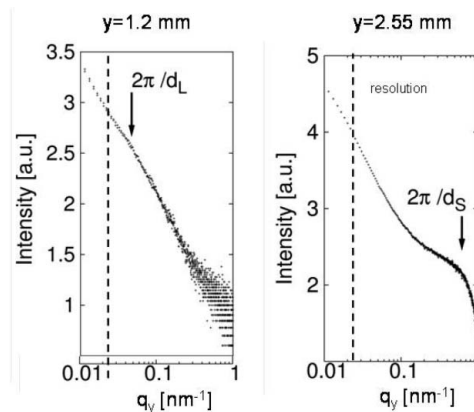

Figure 5
Out-of-plane cuts for the corresponding two-dimensional μGISAXS pattern in Fig. 4(a; insets). At y = 1.2 mm the largest, at y = 2.55 mm the smallest most prominent in-plane length scales are marked by arrows. The dashed vertical lines represent the resolution.

solution. Due to evaporation, the evolving colloidal solution film has its smallest thickness due to evaporation between the barrier and the drop position. Hence, the capillary forces are strongest when the thickness t_W of the water film is in the order of the nanoparticle size ($t_W \sim 5$–10 nm). It drives the gold nanoparticles away from the barrier and from the drop. According to this model, a maximum concentration will be established at a certain distance from the barrier at $y = 0$ mm. In Fig. 4(a) its onset can be estimated at $y = 0.3$ mm and its extension to 0.45 mm. Between $y = 0.3$ mm and $y = 0.45$ mm in the grey shaded area in Fig. 4(a), we determine a coexistence region of the two length scales d_L and d_S. This can be explained in according to Fig. 4(b). Firstly, for $y < 0.3$ mm the individual nanoparticles are largely separated [Fig. 4(b), left]. Between 0.15 mm $< y <$ 0.6 mm [grey shaded region in Fig. 4(a)] domains of nanoparticles have formed. Still, they are centred around nuclei having a distance d_L. Inside these domains the nanoparticles are packed at a distance of approximately 10 nm [Fig. 4(b), middle]. This explains the appearance of the second length scale d_S. Finally, these domains coalesce. Only the length scale d_S is prevailing [Fig. 4(b), right]. Scanning further towards the initial drop position, we see that a second transition at $y = 0.9$ mm to large separations occurs. At $y = 1.8$ mm, the structure oscillates back to a layer with nanoparticle distance d_S. Thus due to hydrodynamic flow a third length scale in the order of several 100 μm becomes evident in addition to the nanoscopic length scales d_S and d_L.

5. Conclusion

Scanning μGISAXS measurements on the one-dimensional gradient of a dried colloidal gold solution are presented. From the μGISAXS pattern we are able to derive two most-prominent length scales, namely d_S (approximately twice the colloid diameter) and d_L (approximately $10 \times d_S$). The latter indicates depleted regions with largely separated nanoparticles. According to a simple hydrodynamic model based on the drying behaviour of colloidal solutions (Govor *et al.*, 2004; Deegan *et al.*, 1997; Deegan, 2000; Denkov *et al.*, 1992; Denkov *et al.*, 1993) the crossover regimes between depleted regions, domain formation and nanoparticle layers can be described qualitatively. Moreover, a new, third length scale in the 100 μm range exists, indicating an oscillation of the structure formation between the three regions (depleted, domains, packed). With respect to future technological applications, the ability to install the reported oscillatory pattern might be useful to tune optical properties of the noble metal layer. Further μGISAXS investigations should include *in-situ* investigations of drying colloidal solution not only at the surface (Narayanan *et al.*, 2004), but at the three-phase-boundary solution–air–substrate. *In-situ* monitoring of the process of nanostructuring induced by the interaction of the noble metal with the substrate is of special interest. Such investigations exploit the *in-situ* possibilities of μGISAXS and might even be combined with nanoscopic beams.

References

Bauer, G., Hassmann, J., Walter, H., Haglmüller, J., Mayer, C. & Schalkhammer, T. (2003). *Nanotechnology*, **14**, 1289–1311.

Bauer, G., Pittner, F. & Schalkhammer, T. (1999). *Mikrochim. Acta*, **131**, 107–114.

Bhat, R. R., Genzer, J., Chaney, B. N., Sugg, H. W. & Liebmann-Vinson, A. (2003). *Nanotechnology*, **14**, 1145–1152.

Deegan, R. D. (2000). *Phys Rev. E*, **61**, 475–485.

Deegan, R. D., Bakajin, O., Dupont, T. F., Huber, G., Nagel, S. R. & Witten, T. A. (1997). *Nature*, **389**, 827–829.

Denkov, N. D., Velev, O. D., Kralchevsky, P. A., Ivanov, I. B., Yoshimura, H. & Nagayama, K. (1992). *Langmuir*, **8**, 3183–3190.

Denkov, N. D., Velev, O. D., Kralchevsky, P. A., Ivanov, I. B., Yoshimura, H. & Nagayama, K. (1993). *Nature*, **361**, 26.

Ditlbacher, H., Krenn, J. R., Lamprecht, B., Leitner, A. & Aussenegg, F. R. (2000). *Opt. Lett.* **25**, 563–565.

Dubertret, B., Calame, M. & Libchaber, A. J. (2001). *Nat. Biotechnol.* **19**, 365–370.

Garell, R. L. (1989). *Anal. Chem.* **61**, 401A–410A.

Gehrke, R. (1992). *Rev. Sci. Instrum.* **63**, 455–458.

Govor, L. V., Bauer, G. H., Reiter, G. & Parisi, J. (2004). *Phys. Rev. E*, **69**, 061609-1–061609-8.

Heer, W. A. de, Selby, K., Kresin, V., Masui, J., Vollmer, M., Chatelain, A. & Knight, W. D. (1987). *Phys. Rev. Lett.* **59**, 1805–1808.

Hulteen, J. C., Patrissi, C. J., Miner, D. L., Crosthwait, E. R., Oberhauser, E. B. & Martin, C. R. (1997). *J. Phys. Chem. B*, **101**, 7727–7731.

Jin, R., Cao, Y., Mirkin, C. A., Kelly, K. L., Schatz, G. C. & Zheng, J. G. (2001). *Science*, **294**, 1901–1903.

Krebs, H.-U., Weisheit, M., Faupel, J., Süske, E., Scharf, T., Fuhse, C., Störmer, M., Sturm, K., Seibt, M., Kijewski, H., Nelke, D., Panchenko, E. & Buback, M. (2003). *Adv. Solid State Phys.* **43**, 505–517.

Lengeler, B., Schroer, C. G., Kuhlmann, M., Benner, B., Günzler, T. F., Kurapova, O., Zontone, F., Snigirev, A. & Snigireva, I. (2005). *J. Phys. D Appl. Phys.* **38**, A218–A222.

Maier, S. A., Brongersma, M. L., Kik, P. G., Meltzer, S., Requicha, A. A. G. & Atwater, H. A. (2001). *Adv. Mater.* **13**, 1501–1505.

Müller-Buschbaum, P. (2003). *Anal. Bioanal. Chem.* **376**, 3–11.

Müller-Buschbaum, P., Bauer, E., Pfister, S., Roth, S. V., Burghammer, M., Riekel, C., David, C. & Thiele, U. (2006). *Europhys. Lett.* **73**, 35–41.

Müller-Buschbaum, P., Roth, S. V., Burghammer, M., Diethert, A., Panagiotou, P. & Riekel, C. (2003). *Europhys. Lett.* **61**, 639–645.

Narayanan, S., Wang, J. & Lin, X.-M. (2004). *Phys. Rev. Lett.* **93**, 135503.

Naudon, A. & Thiaudière, D. (1996). *Surf. Coat. Technol.* **79**, 103–107.

Park, S. H. & Xia, Y. (1999). *Langmuir*, **15**, 266–273.

Revenant, C., Leroy, F., Lazzari, R., Renaud, G. & Henry, C. R. (2004). *Phys. Rev. B*, **69**, 305411.

Roth, S. V., Burghammer, M., Riekel, C., Müller-Buschbaum, P., Diethert, A., Panagiotou, P. & Walter, H. (2003). *Appl. Phys. Lett.* **82**, 1935–1937.

Roth, S. V., Döhrmann, R., Dommach, M., Kuhlmann, M., Kröger, I., Gehrke, R., Walter, H., Schroer, C. G., Lengeler, B. & Müller-Buschbaum, P. (2006). *Rev. Sci. Instrum.* **77**, 085106.

Roth, S. V., Müller-Buschbaum, P., Burghammer, M., Walter, H., Panagiotou, P., Diethert, A. & Riekel, C. (2004). *Spectrochim. Acta Part B*, **59**, 1765–1773.

Roth, S. V., Walter, H., Burghammer, M., Riekel, C., Lengeler, B., Schroer, C., Kuhlmann, M., Walther, T., Sehrbrock, A., Domnick, R. & Müller-Buschbaum, P. (2006). *Appl. Phys. Lett.* **88**, 021910.

Salditt, T., Metzger, T. H., Brandt, C., Klemradt, U. & Peisl, J. (1995). *Phys. Rev. B*, **51**, 5617–5627.

Schmid, G. & Chi, L. F. (1998). *Adv. Mater.* **10**, 515–526.

Schroer, C. G., Kuhlmann, M., Roth, S. V., Gehrke, R., Stribeck, N., Almendarez-Camarillo, A. & Lengeler, B. (2006). *Appl. Phys. Lett.* **88**, 164102.

Stenzel, O., Stendal, A., Voigtsberger, K. & von Borczyskowski, C. (1995). *Sol. Energy Mater. Sol. Cells*, **37**, 337–348.

Su, P. Y., Hu, J. C., Cheng, S. L. & Chen, L. J. (2004). *Appl. Phys. Lett.* **84**, 3480–3482.

Taton, T. A., Mirkin, C. A. & Letsinger, R. L. (2000). *Science*, **289**, 1757–1760.

Vo-Dinh, T., Stokes, D. L., Griffin, G. D., Volkan, M., Kim, U. J. & Simon, M. I. (1999). *J. Raman Spectrosc.* **30**, 785–793.

Westphalen, M., Kreibig, U., Rostalski, J., Lüth, H. & Meissner, D. (2000). *Sol. Energy Mater. Sol. Cells*, **61**, 97–105.

Yoneda, Y. (1963). *Phys. Rev.* **131**, 2010–2013.

Zeman, E. J. & Schatz, G. C. (1987). *J. Chem. Phys.* **91**, 634–643.